ARIES-ACT-1 Plasma Disruption Magnetic and Structural Analysis

C.J. Martin and J.P. Blanchard

February 2014

UWFDM-1417

FUSION TECHNOLOGY INSTITUTE

UNIVERSITY OF WISCONSIN

MADISON WISCONSIN

ARIES-ACT-1 Plasma Disruption Magnetic and Structural Analysis

C.J. Martin and J.P. Blanchard

Fusion Technology Institute
University of Wisconsin
1500 Engineering Drive
Madison, WI 53706

http://fti.neep.wisc.edu

February 2014

UWFDM-1417

ARIES-ACT-1 PLASMA DISRUPTION MAGNETIC AND STRUCTURAL ANALYSIS

C. J. Martin and J. P. Blanchard

Fusion Technology Institute, University of Wisconsin, Madison, WI, cjmartin@engr.wisc.edu

Introduction

Calculations were performed to estimate the electromagnetic forces and stresses in the vacuum vessel of the ARIES-ACT-1[1] device resulting from plasma disruption events. Specifically, the model presented here simulates a stationary plasma in which the current decreases linearly over a 30 ms time period. Other events, such as a vertical displacement or halo current, are left for future projects. The current quench induces large electrical currents in the conductive components of the device. These currents interact with the existing magnetic field to produce potentially large magnet forces on the components. Only the toroidally continuous components—the vacuum vessel, vertical stabilizing shells, and structural ring—were considered. All other structures were ignored in order to simplify the model. The poloidal and toroidal field coils remained energized during the disruption at peak current and field levels. Magnetic finite element analyses are used to calculate the transient induced currents and magnetic forces within the conducting structures. These magnetic body forces are then applied as time dependent loads to transient structural analysis models of the vacuum vessel.

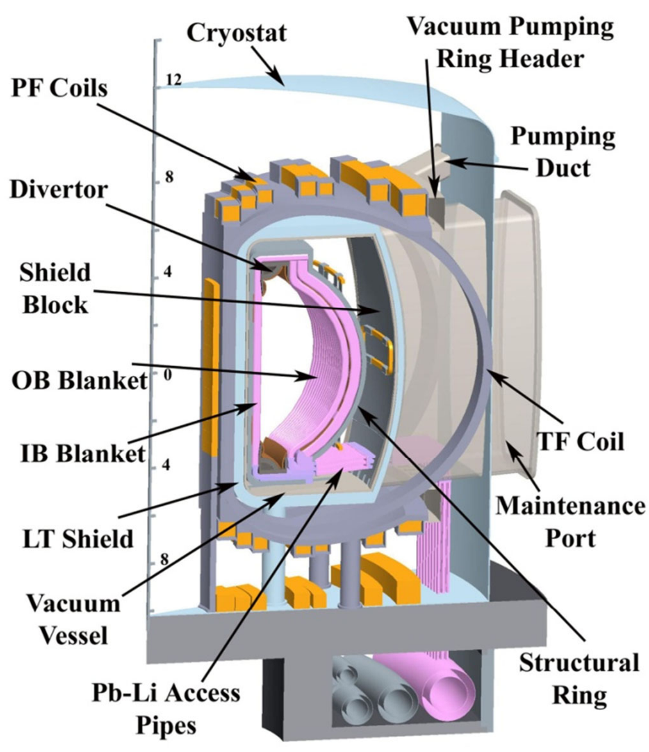

Fig. 1. Isometric view of one sector of the ARIES-ACT-1 power core.

Finite Element Model

The ARIES-ACT vacuum vessel[3] has sixteen access ports regularly spaced. The CAD model of the vacuum vessel[2] provided was for a 22.5° segment with a uniform wall thickness of 10 cm, and vertical symmetry was used to further reduce the model size. The volume surrounding the tokamak was modeled, as vacuum, to a radius of 27 m. In addition to the vacuum vessel, the model includes representations of significant toroidally continuous conduction paths (the steel structural ring and tungsten stabilizing shells, as shown in Fig. 2), the toroidal and poloidal magnetic coils, and the plasma. All analysis and modeling was performed using the commercial finite element code ANSYS. The model geometry and FE mesh are illustrated in Fig. 2. The model contains over 6 million nodes and over 4 million 3-D, 10-node, electromagnetic solid elements.

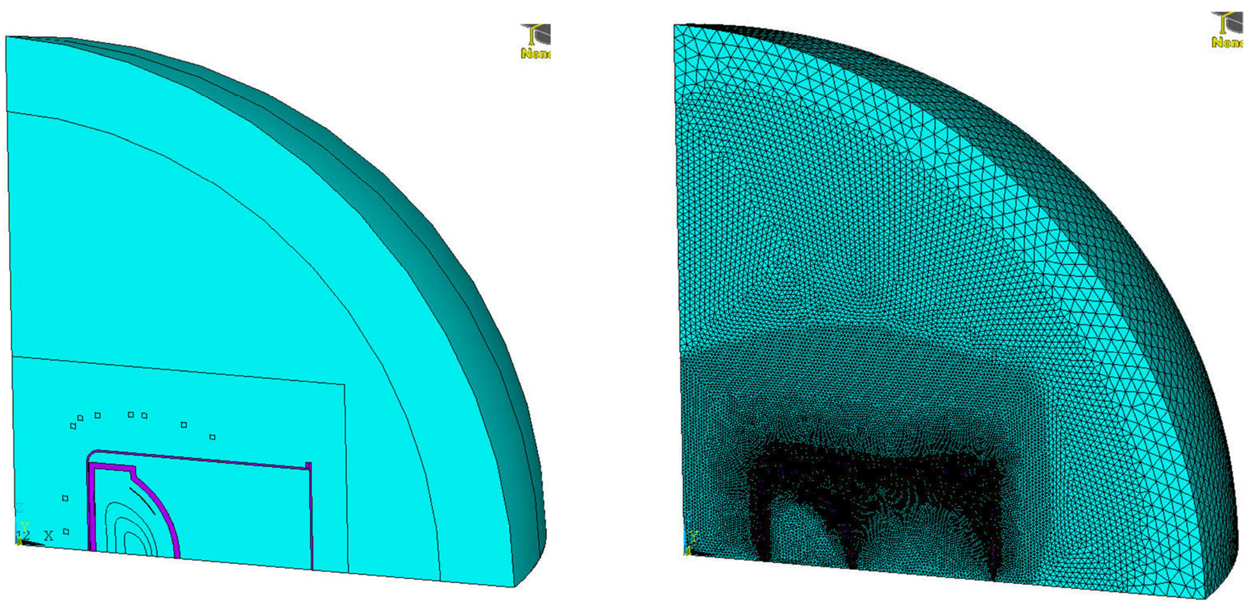

(a) (b)

Fig. 2. The modeled region showing significant features (a) and the finite element mesh (b) used in the magnetic analysis.

A significant limitation of using only an angular sector of the full geometry to model is that it is not possible to model the magnetic fields produced by the poloidal field (PF) coils and plasma and the toroidal field (TF) coils. The PF coils and plasma require flux parallel boundary conditions on the circumferential faces while the TF coils require flux normal boundaries and do not allow the vertical symmetry shown. The magnetic forces resulting from the induced currents in the vacuum vessel after plasma shutdown were calculated in separate analyses for the poloidal and toroidal field coils. These forces were then summed for use as inputs in the structural analyses. The components of interest are illustrated in Fig. 3. Appropriate source currents are applied to the field coils. The currents used in these analyses are the maximum current expected in each coil and are assumed to travel in the same direction as the plasma current. The locations and currents in the various coils are provided in Table 1. The magnetic flux density produced by the poloidal field coils is shown in Fig. 4. For comparison, the toroidal field design point is a 5.5 T field at a radius of 5.5 m.

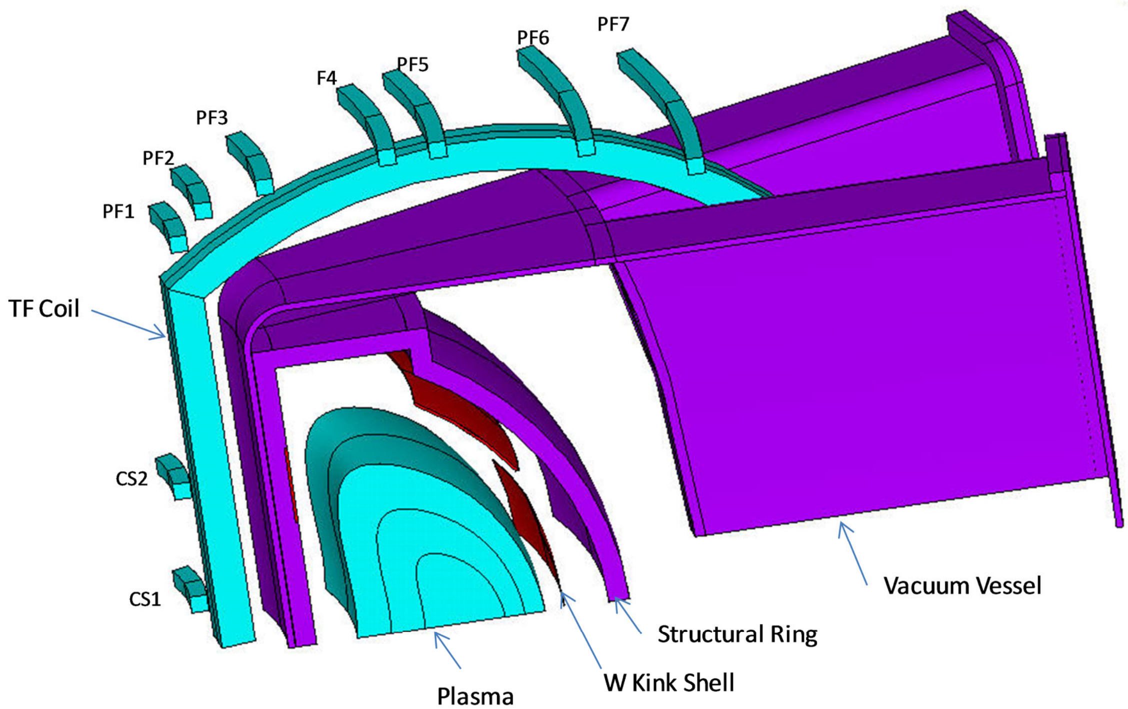

Fig. 3. Major components included in the model.

Table 1. Location of poloidal field coils and their currents

Coil	R (m)	Z (m)	Imax (MA)
CS1	2.75	0.9	4.5
CS2	2.75	2.7	6.8
PF1	3.23	6.57	8.05
PF2	3.91	7.03	5.54
PF3	4.58	7.26	5.46
PF4	6.39	7.45	6.62
PF5	7.13	7.45	6.62
PF6	9.25	7.15	8.45
PF7	10.78	6.61	14.4

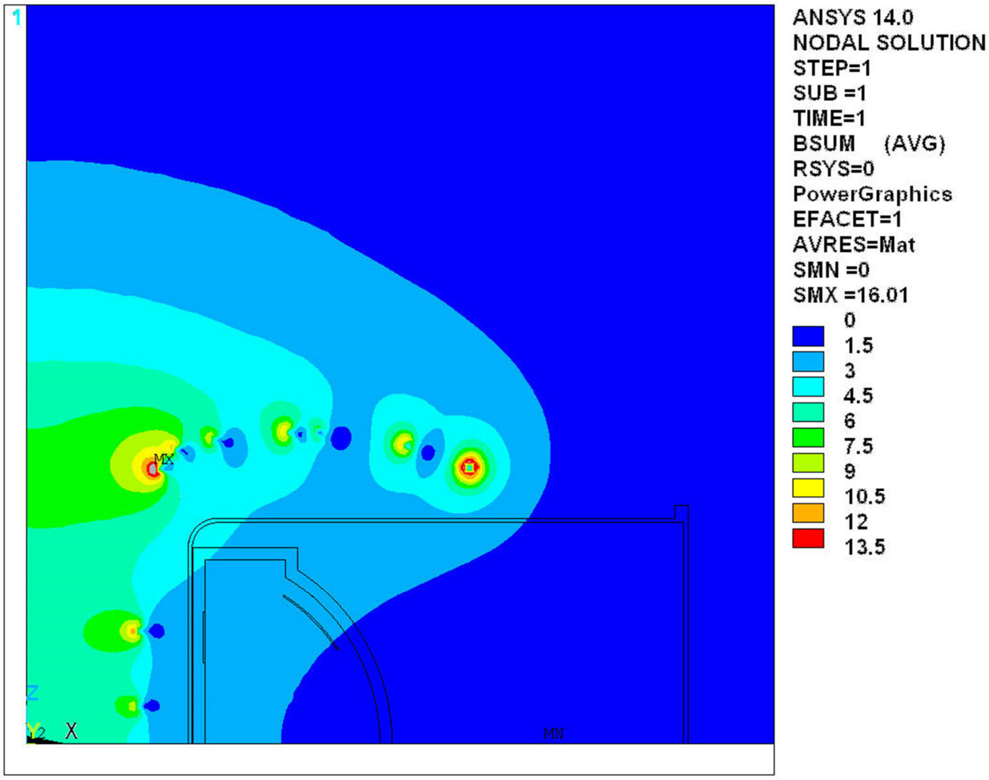

Fig. 4. Total magnetic flux density (B, T) produced by the poloidal field coils.

The total plasma current of 10.9 MA was applied to the volumes designated as plasma in Fig. 3 with different current densities in each of the three plasma regions to simulate the actual plasma shape. In the transient magnetic analyses presented here, the plasma is assumed to be running at steady state at t=1.0 s, at which time the plasma is ramped down to zero current over a time interval of 0.03 s. The changing field induces currents in the conductive components. The plasma initially produces the magnetic field shown in Fig. 5 which ramps down with the current at the beginning of the transient. For the ferritic steel components, the vacuum vessel and structural ring, an electrical resistivity of 7.5 x 10^{-7} Ω-m was used. For the tungsten components, a resistivity of 3.3 x 10^{-7} Ω-m was used. In these analyses the magnetic behavior of the ferritic steel was ignored, and the permeability of all regions was set to 1.0. Later analyses, which used B-H curves for a magnetic ferritic steel alloy, showed no significant change in induced currents from the magnetic transients.

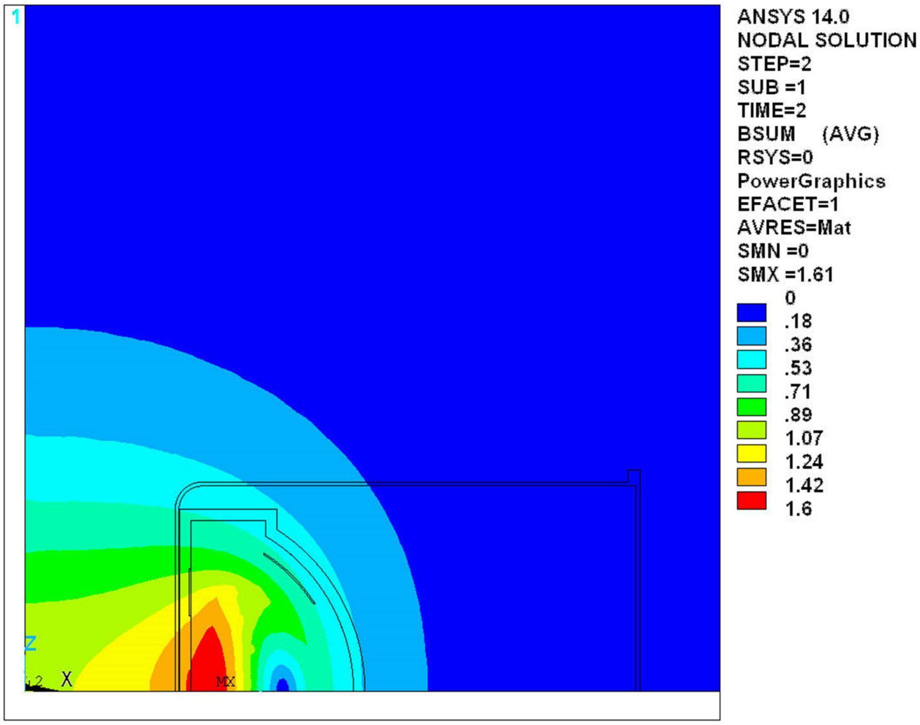

Fig. 5. Total magnetic flux density (B, T) produced by the 10.9 MA plasma current.

Transient Magnetic Analysis – Poloidal Field Coils

The plasma disruption event modeled assumes a linear ramping down of the plasma current over a time of 0.03 s. In the magnetic transient analysis, the plasma and coil currents and their magnetic fields are operating at steady state at time t=1.0 s. The plasma current is then ramped down, and at time t=1.03 s the plasma current is zero, but the current in the poloidal field coils is maintained. The magnetic field produced by the plasma current (Fig. 5) also ramps down, and the change in this field induces currents in the conducting reactor components. The current flow at the end of the plasma ramp down is illustrated in Fig. 6. In general, the currents flow toroidally around the device. The exceptions are the discontinuous kink shell, where the currents flow around the perimeter, and the outboard vacuum vessel where the relatively small currents must flow around the maintenance ports. The magnitudes of the current densities as a function of time in the various components are illustrated in Fig. 7. Note that the currents in the structural ring and tungsten shell peak at the end of plasma ramp down (t=1.03 s) while the current in the vacuum vessel has a much longer rise time. The currents and magnetic nodal forces in the structural ring (in Fig. 8) and the tungsten components (Fig. 9) are illustrated at the end of plasma ramp down. It is important to note that these magnetic forces do not contain contributions from the toroidal field coils, and that their magnitude is dependent on the FE mesh size (because the force on an element depends on the volume of the element). Nonetheless, they provide insight into the direction and relative magnitudes (the mesh is fairly uniform) of the induced magnetic forces.

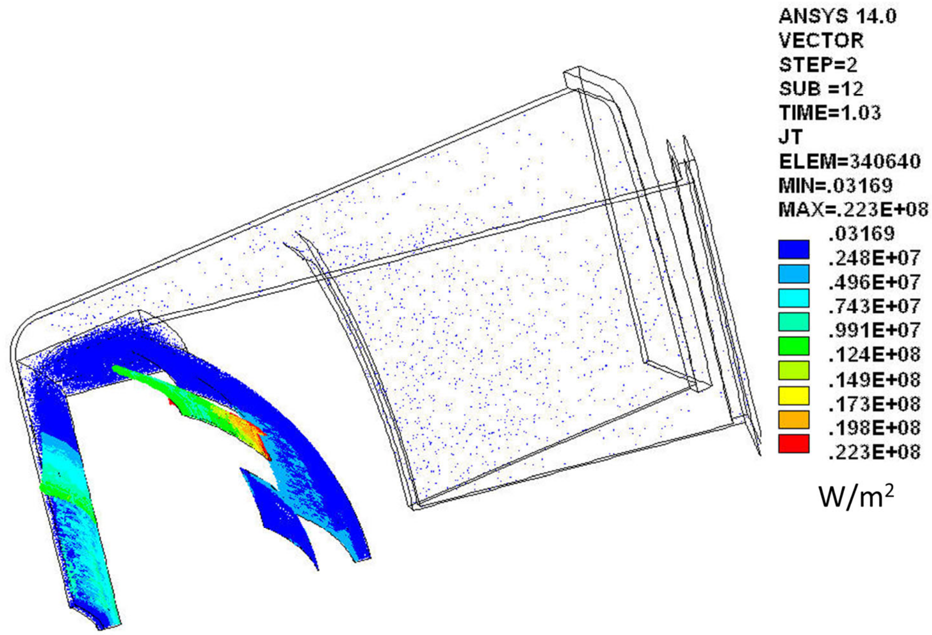

Fig. 6. Induced current densities at the end of plasma ramp down (t=1.03 s).

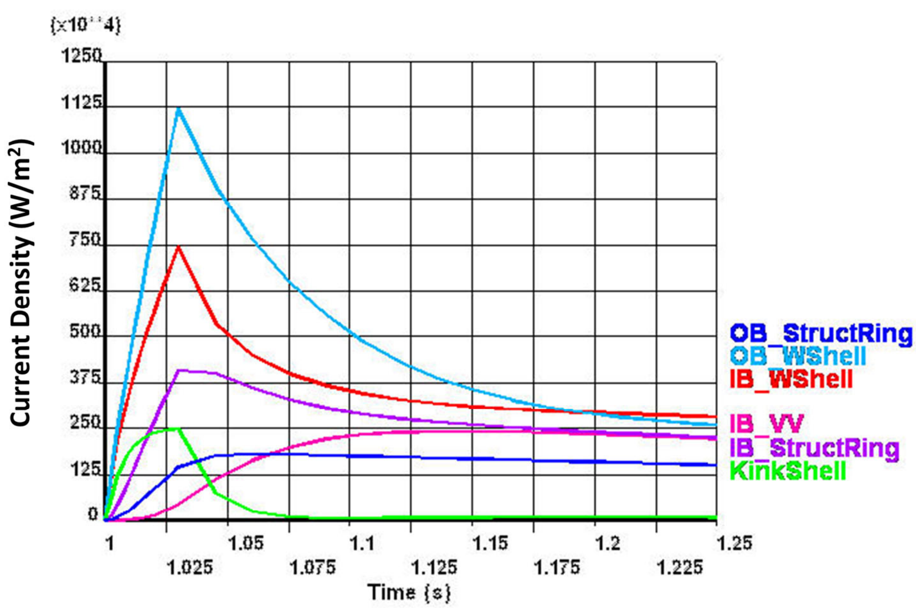

Fig. 7. Induced current densities in the various modeled components after plasma disruption.

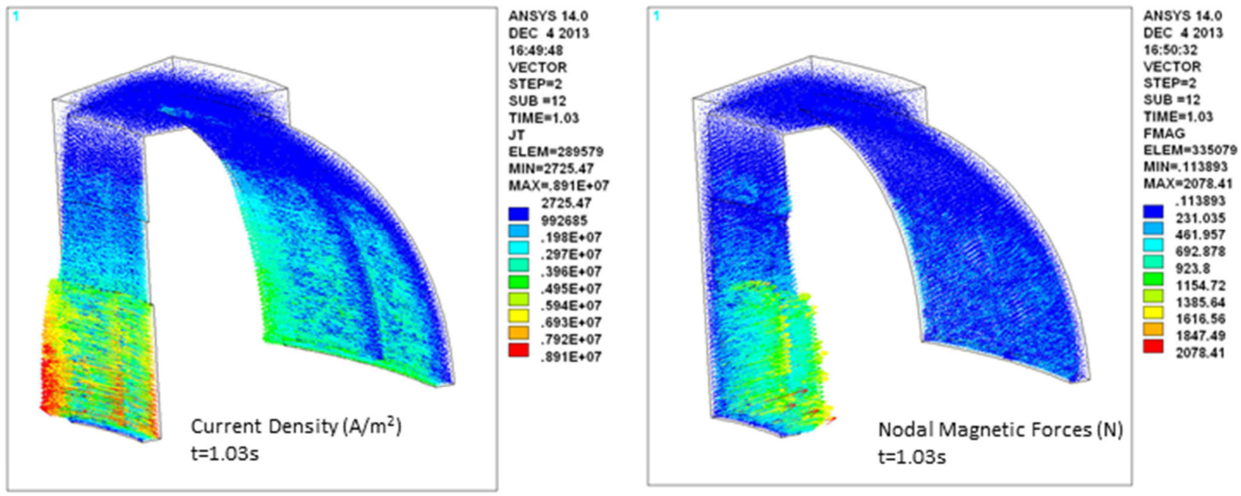

(a) (b)

Fig. 8. Currents (a) and nodal magnetic forces (b) in structural ring at the end of the plasma ramp down.

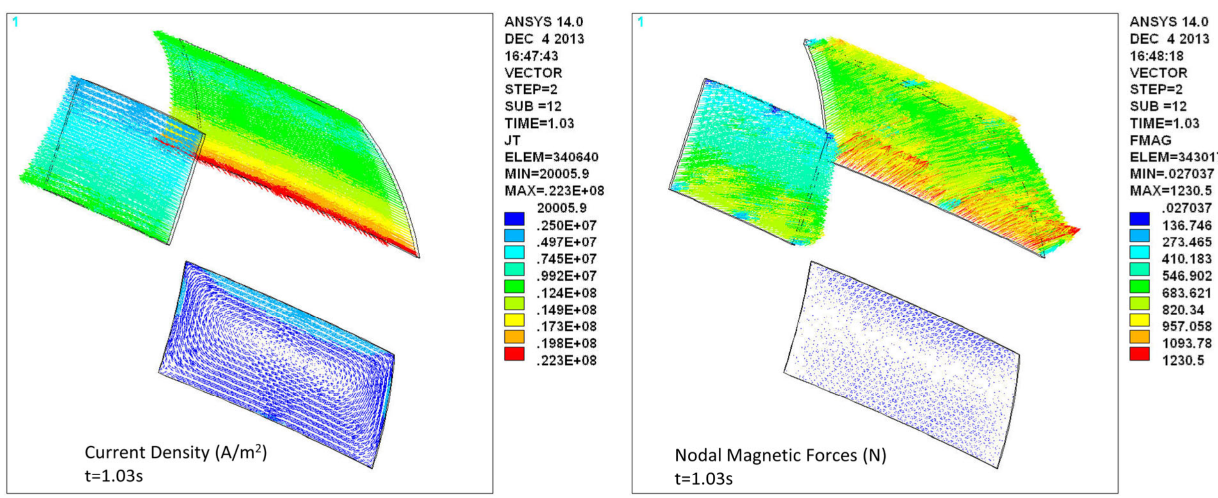

(a) (b)

Fig. 9. Currents (a) and nodal magnetic forces (b) in the tungsten components at the end of the plasma ramp down.

As mentioned previously, currents rise more slowly in the vacuum vessel and reach a gradual peak approximately 0.10 seconds after the end of the plasma quench event. Induced currents at several points in the vacuum vessel as a function of time are shown in Fig. 10. The induced current densities and magnetic nodal forces are displayed at times t=1.03 s, t=1.10 s, and t=1.15 s in Figs. 11-13. These figures illustrate how the currents and magnetic forces are highest on the inboard region of the vacuum vessel near the centerline, and the forces in the outboard vacuum ports are relatively small.

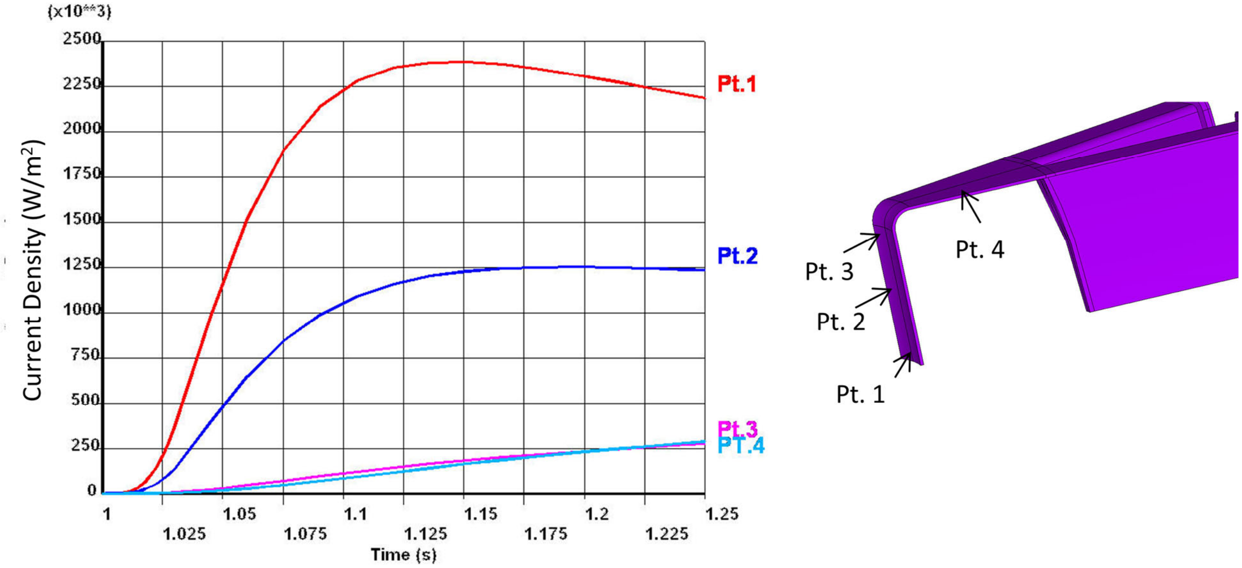

Fig. 10. Induced current densities in the vacuum vessel after plasma disruption.

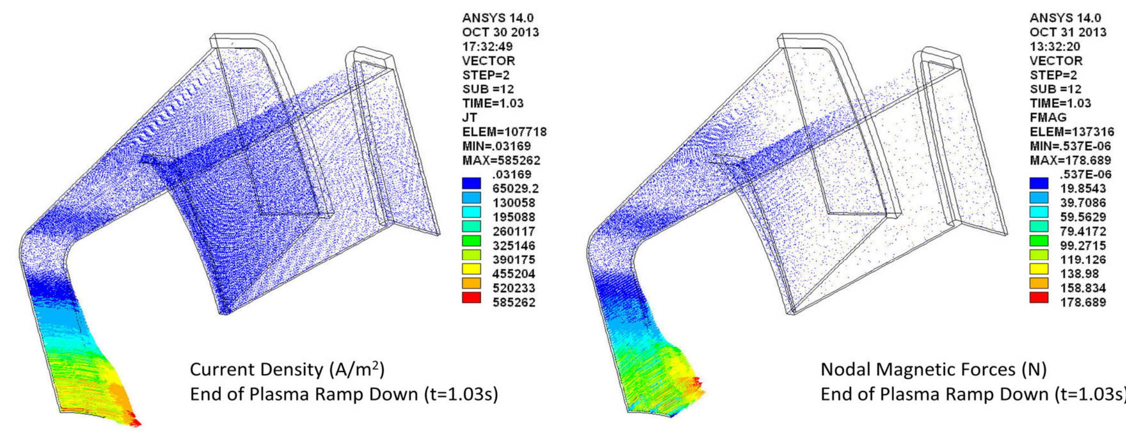

(a) (b)

Fig. 11. Currents (a) and nodal magnetic forces (b) in the vacuum vessel at the end of the plasma ramp down (t=1.03 s).

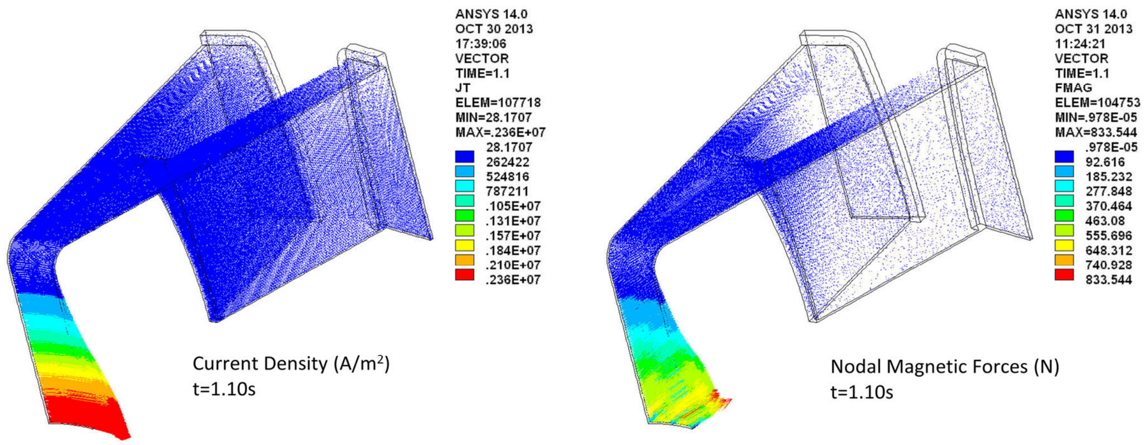

(a) (b)

Fig. 12. Currents (a) and nodal magnetic forces (b) in the vacuum vessel at t=1.10 s.

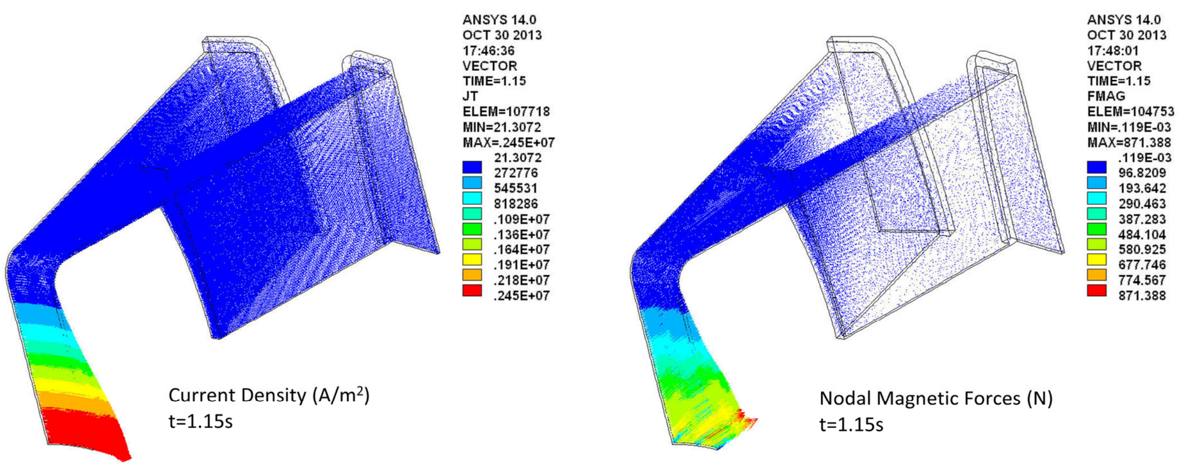

(a) (b)

Fig. 13. Currents (a) and nodal magnetic forces (b) in the vacuum vessel at t=1.15 s.

While the calculated nodal forces can be directly imported to the ANSYS structural finite element model, they are less than ideal for results interpretation because these forces are a function of the element sizes to which the node is attached. In order to produce a more usable output, a plot of magnetic body force was produced dividing the total magnetic force on each element by its volume. The results of this calculation at t=1.15 s for the radial body force are shown in Fig. 14. As can be seen the body forces are the highest on the inboard wall and decrease with distance from the symmetry centerline. The radial body force as a distance from the centerline is shown in Fig. 15 at t=1.10 s and t=1.15 s. The shape and magnitude of the distributions are quite similar at the two time points and little variation is seen through the thickness. Plots of the magnetic body forces in the structural ring and tungsten shells at the end of plasma ramp down may be found in appendix 3.

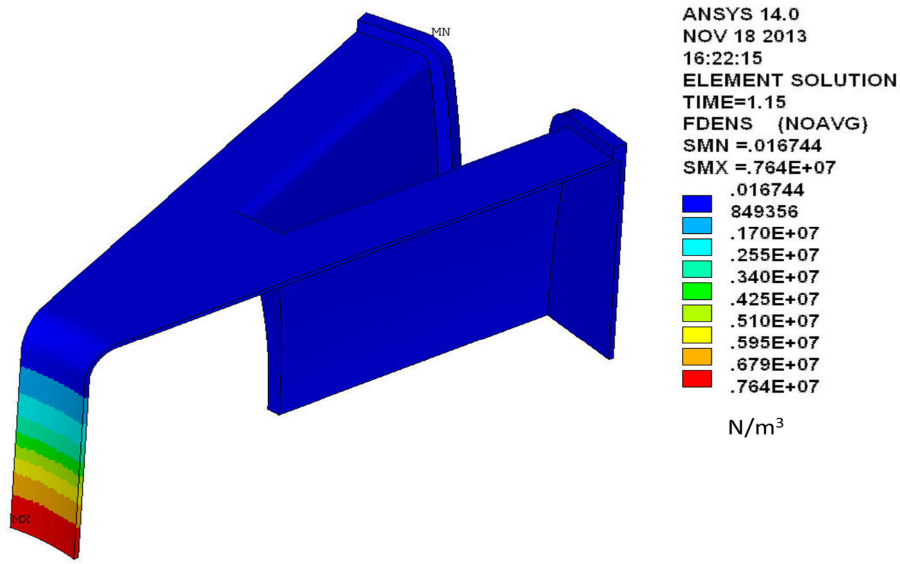

Fig. 14. Radial magnetic body force on vacuum vessel at t=1.15 s.

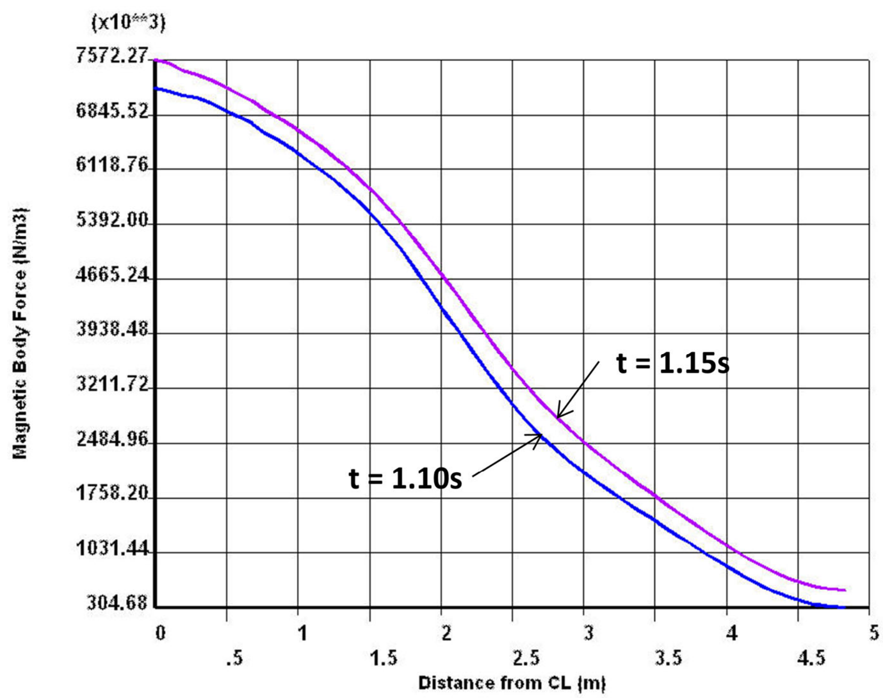

Fig. 15. Radial magnetic body force on the inner wall of vacuum vessel as a function of the distance from the symmetry centerline at t=1.10 s and t=1.15 s.

Transient Magnetic Analysis – Toroidal Field Coils

The magnetic fields produced by the toroidal field coils cannot be simulated with the finite element model used in the previous analyses. First, the current flow in the coils is not symmetric about the vertical centerline thus requiring reflection of the model about this plane. Secondly, the boundary conditions and the sector symmetry faces must be changed from flux parallel to flux normal. The latter condition precludes the modeling of both the plasma current and the toroidal field coil currents in the same magnetic analysis using only a sector of the model. Since modeling the entire device was not feasible with the given computer resources, the following procedure was developed to predict the magnetic forces in the vacuum vessel produced by the interaction of the fields produced by the TF coils and the currents induced by plasma disruption. First, the FE mesh used in the previous analyses was reflected across the vertical symmetry plane, flux normal boundary conditions applied to the sector faces and the TF coil currents applied. Because the magnetic fields produced by the TF coils should not be affected by the plasma disruption, a static magnetic analysis of the fields produced was conducted. The results of this are shown in Fig. 16. This field was then applied as nodal constraints to a magnetic model of the upper half of the vacuum vessel. The time dependent current densities in the vacuum vessel were then applied as loads to this model and the magnetic nodal forces computed at each time step. The magnetic forces in the vacuum vessel produced by the fields from the TF coils are illustrated in Fig. 17. The largest forces again are in the inboard region where the induced currents are highest but the force direction is in the plane of the wall. Forces in this region were not initially expected as the current and field lines run essentially parallel to one another so **J**×**B** forces would be small. Closer examination of the fields showed a variation in the radial component of the field in the vacuum vessel wall which produced these forces (Fig. 18).

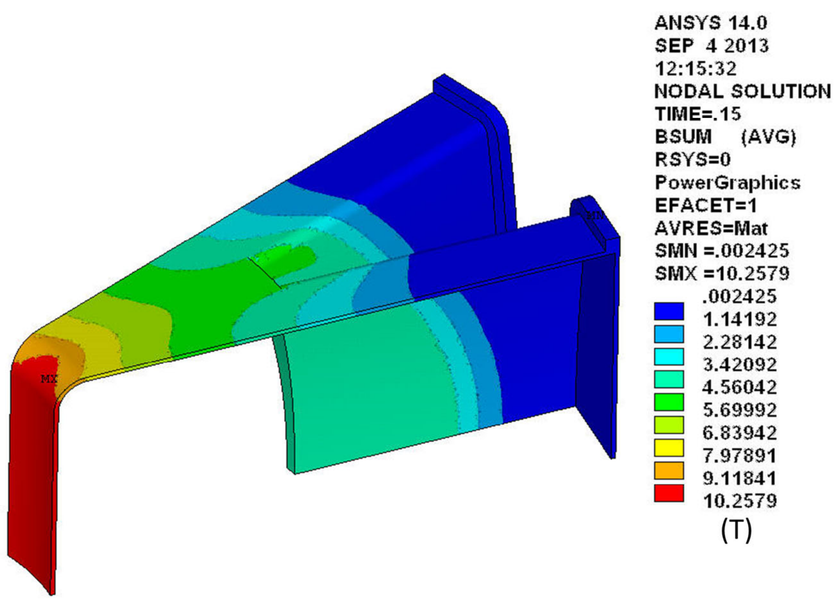

Fig. 16. Total magnetic flux density (B, T) in the vacuum vessel produced by the toroidal field coils.

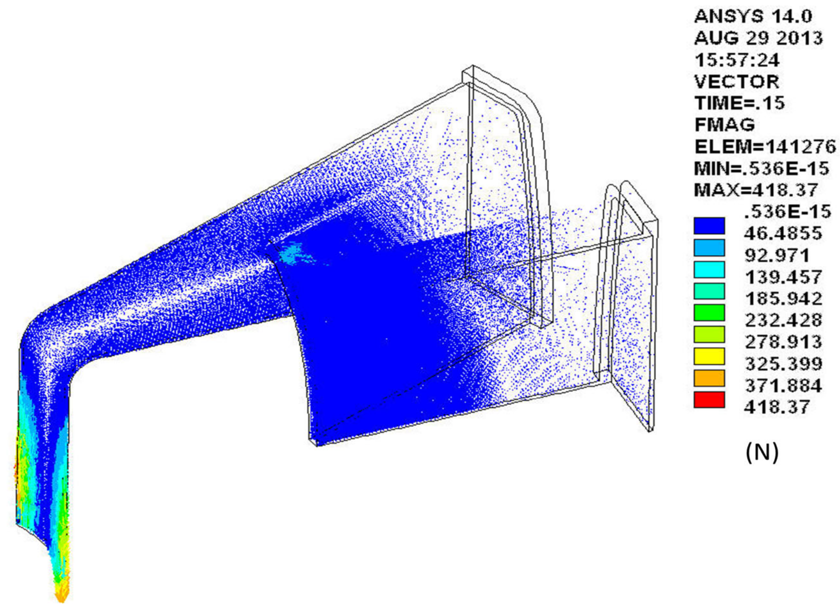

Fig. 17. Nodal magnetic forces produced by the TF coils in the vacuum vessel at t=1.15 s.

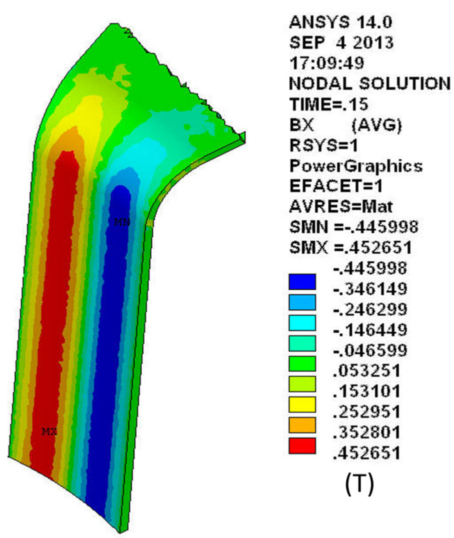

Fig. 18. Radial component of magnetic flux (B_r, T) in vacuum vessel inner wall.

Vacuum Vessel Transient Structural Analysis

Of primary interest in these analyses are the stresses induced in the vacuum vessel by forces resulting from a plasma disruption. To this end, a structural FE model of the 10 cm thick solid vacuum vessel was created using the same mesh numbering as the magnetic model. This facilitated data transfer between models in ANSYS. For the transient analysis, the magnetic force results produced by the PF and TF coils were imported and summed at each time point in the magnetic analysis. The only applied boundary conditions were the symmetry conditions. The structural supports were not modeled and neither were any structural or thermal loads that might be encountered during normal operation. For the structural analyses, the plasma disruption begins at t=0.0 s rather than t=1.0 s in the magnetic analysis. The von Mises equivalent stress distribution in the vacuum vessel is illustrated in Fig. 19 at time t=0.15 s. The transient stress responses of three points on the symmetry centerline are shown in Fig. 20. Note that there is some variation across the width of the section resulting from the inclusion of the forces from the TF coils. Also, aside from some higher frequency vibrational response, the stress levels correspond closely to the transient response of the induced currents in the same region. Also of note, the stress and displacement results from the transient analysis were within 5% of the results of a static analysis with the loads at that time point. Looking more closely at the stress results, the highest stresses occur at the juncture between the access ports as illustrated in Fig. 21. This model shows stresses in excess of 90 MPa in this region, but the FEA results in this region are questionable due to faceting of some of the small fillets due to the relatively coarse meshing used. Nonetheless, stresses in this region should be examined closely during the vacuum vessel detailed design.

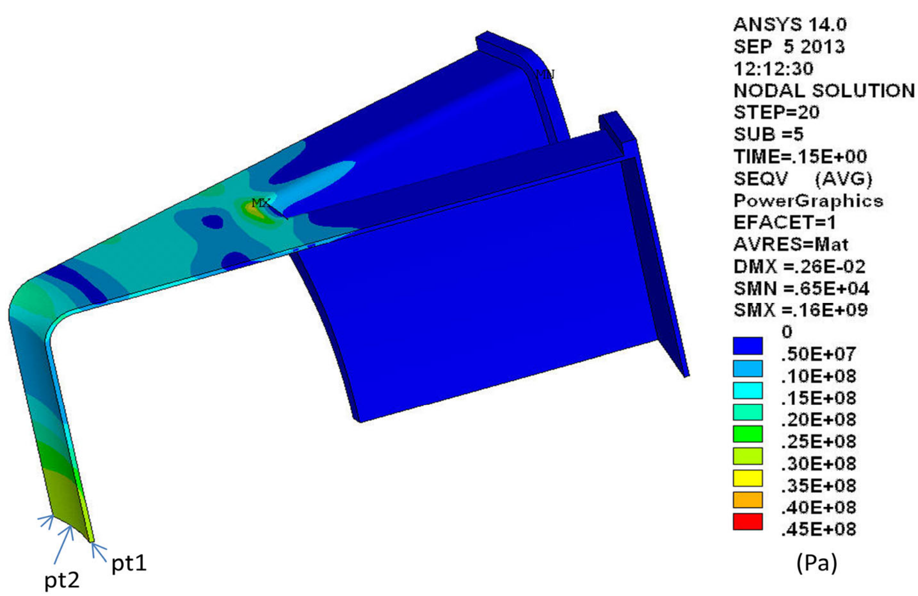

Fig. 19. Equivalent (von Mises) stress in vacuum vessel 0.15 s after start of plasma disruption.

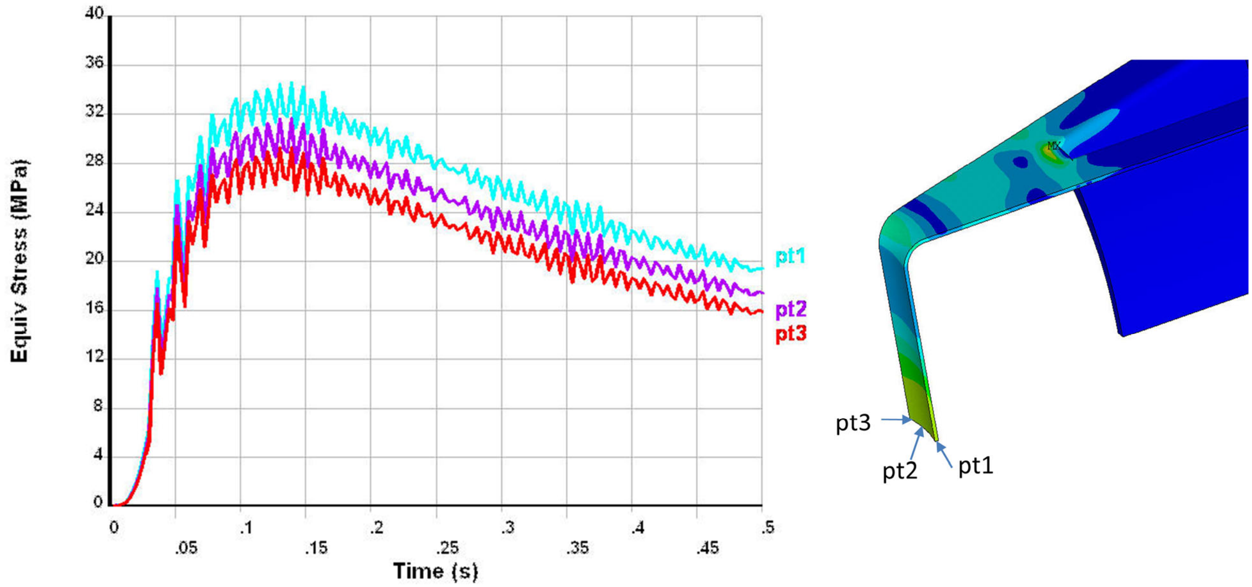

Fig.20. Time dependent equivalent (von Mises) stress at three points on the vacuum vessel vertical centerline.

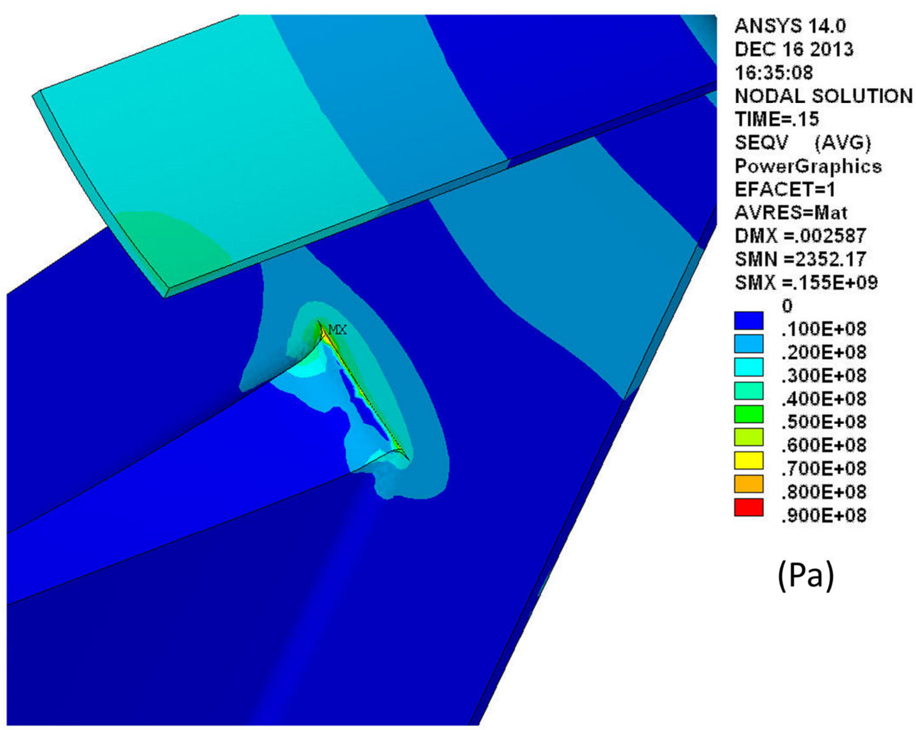

Fig. 21. Equivalent (von Mises) stress in vacuum vessel 0.15 s after start of plasma disruption highlighting the region of maximum stress.

Summary

Transient magnetic and structural analyses have been conducted to simulate a plasma disruption event for the ARIES-ACT-1 power core. The changing magnetic fields resulting for the linear ramp down of the 10.9 MA plasma current over 0.03 s induces currents in the conductive elements of the power core. Only the toroidially continuous structural elements were modeled as these were expected to see the highest induced currents. In addition, to reduce computational time the magnetic properties of the ferritic steel components were ignored. These assumptions were evaluated by including simple blanket modules (appendix 1) and typical ferritic steel magnetic properties (appendix 2) and shown to be valid. Vacuum vessel geometry was obtained from simplified CAD models with 10 cm constant thickness walls as including the cooling passages and other structural details would be computationally prohibitive. Results show that the largest induced currents and magnetic forces occur at the inner wall of the vacuum vessel at approximately 0.15 s after the start of the plasma disruption. These magnetic forces and resulting stresses will have to be accounted for in the overall structural design of the vacuum vessel.

Appendix 1. Induced Currents with Simulated Blanket Modules

One of the modeling assumptions made was to ignore structure that was not electrically continuous around the toroid. Of the structures ignored, the blanket modules which lie between the plasma and modeled structure would have the greatest potential effect on the induced currents in the vacuum vessel. The blanket modules consist of liquid lithium lead (~87%) circulating through a silicon carbide structure. The lithium lead has a relatively high electrical conductivity while the thermal conductivity of the silicon carbide is relatively low, and to accurately predict the induced currents would require discrete modeling of Li-Pb and silicon carbide which is beyond the scope of these studies. To gauge the effect of the blankets, the blankets were simulated with solid blocks of conductive material occupying the space where the blankets would be, as illustrated in Fig. A1. These were given the electrical conductivity of steel which is between that of lithium lead and silicon carbide. The blocks are not electrically continuous toroidally around the device.

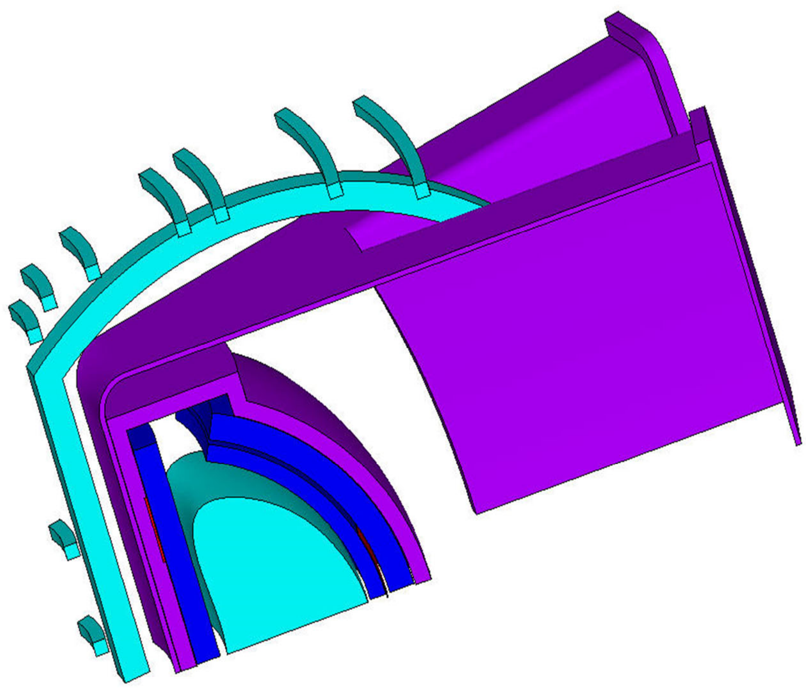

Fig. A1. Model geometry with solid blocks added to simulate blanket modules (dark blue).

The transient magnetic analysis was repeated for this model. The transient current densities at the inboard vacuum vessel center symmetry line are compared for this model and the previous model without the blanket and are shown in Fig. A2. The presence of the simulated blankets slightly reduces peak currents and nodal magnetic forces (Fig. A3). These results indicate that ignoring the blanket will only have a small effect on the structural results and that the assumption should prove to be conservative.

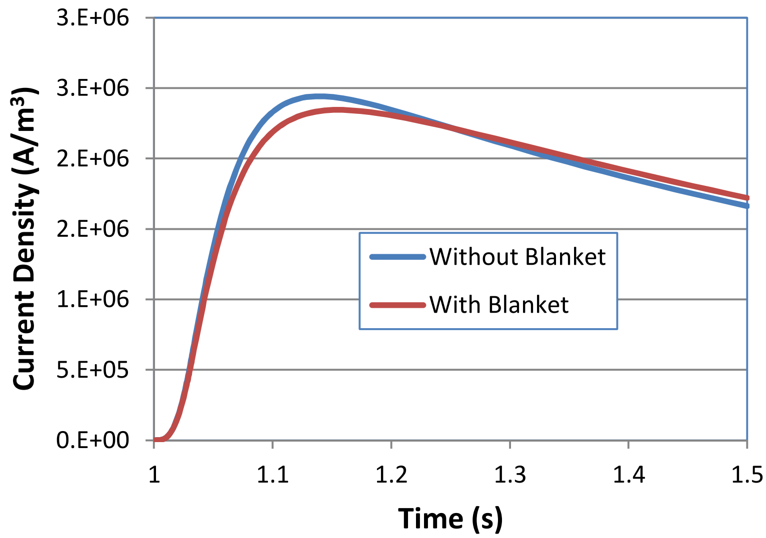

Fig. A2. Current density at vacuum vessel inboard centerline with and without simulated blanket.

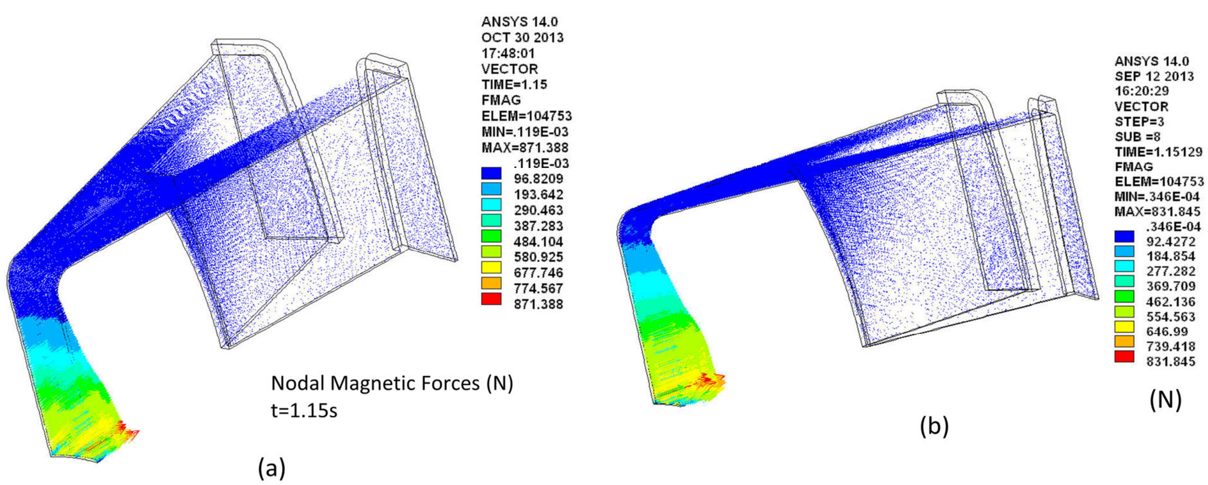

Fig. A3. Nodal magnetic forces without (a) and with (b) simulated blanket at time t=1.15 s.

Appendix 2. Investigation of the Effects of the Inclusion of the Magnetic Properties of Ferritic Steel on the Induced Currents and Magnetic Forces in the Vacuum Vessel

The modeling and results ignored the magnetic qualities of the ferritic steel in the structural ring and vacuum vessel in order to simplify and speed up the calculations. While this assumption was not expected to markedly affect the results as the magnetic fluxes were well above saturation levels, further investigation was warranted. To this end, magnetic properties of the ferritic steel alloy SS430 were included in the model and assigned to the vacuum vessel and structural ring. Alloy SS430 has a saturated magnetization in the range of 1.65 T, and is used in the ferromagnetic inserts in the ITER device.[4] The transient magnetic analysis was then repeated with the poloidal field coils energized. The transient current densities at the inboard vacuum vessel center symmetry line are compared for this model and the previous model and are shown in Fig. A4. The inclusion of the magnetic properties for the ferritic steel slightly reduces peak currents and nodal magnetic forces (Fig. A5). These results indicate that ignoring the magnetic material properties of the ferritic steel has a small effect on the structural forces and it should be noted that including the magnetic properties significantly increased the analysis time.

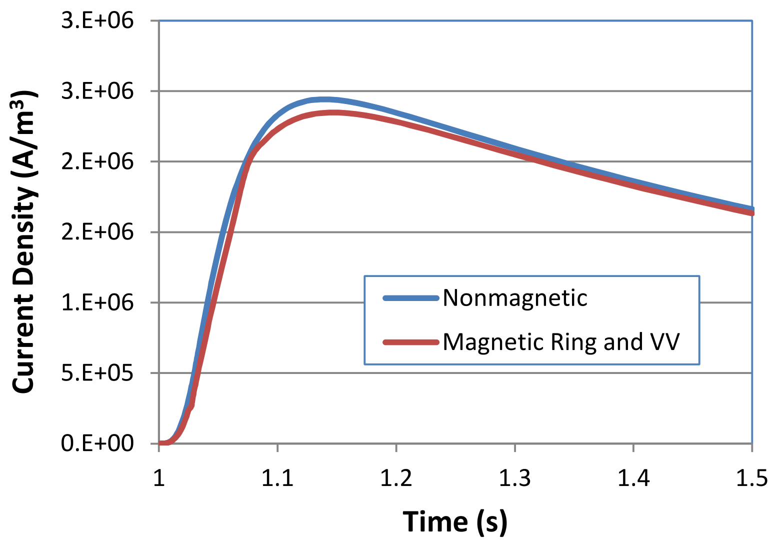

Fig. A4. Current density at vacuum vessel inboard centerline with and without inclusion of magnetic properties for the structural ring and vacuum vessel.

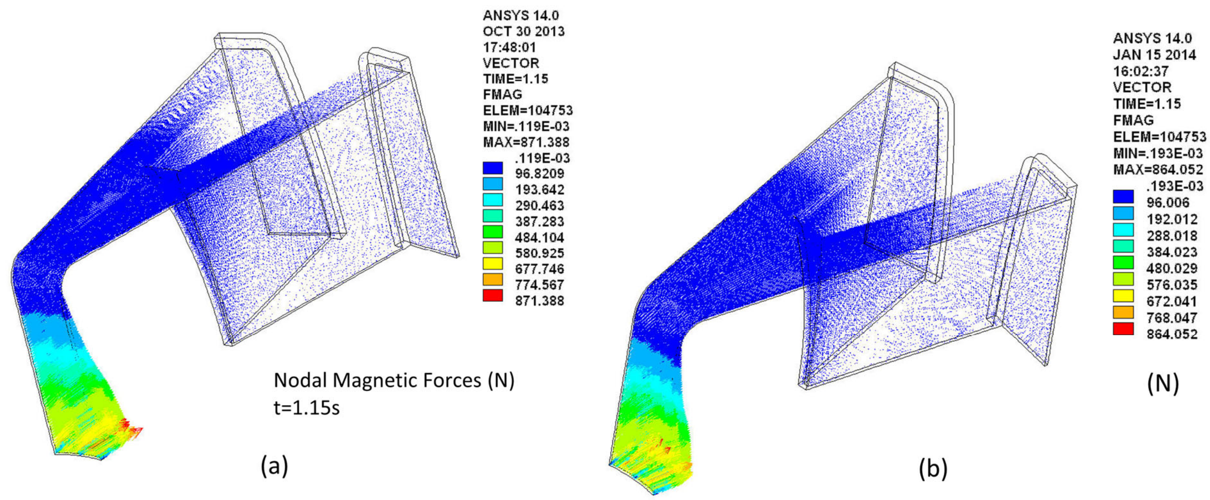

Fig. A5. Nodal magnetic forces without (a) and with (b) magnetic properties for the structural ring and vacuum vessel at time t=1.15 s.

Appendix 3. Body Forces on Structural Ring and Stabilizing Ring at the End of Plasma Ramp Down

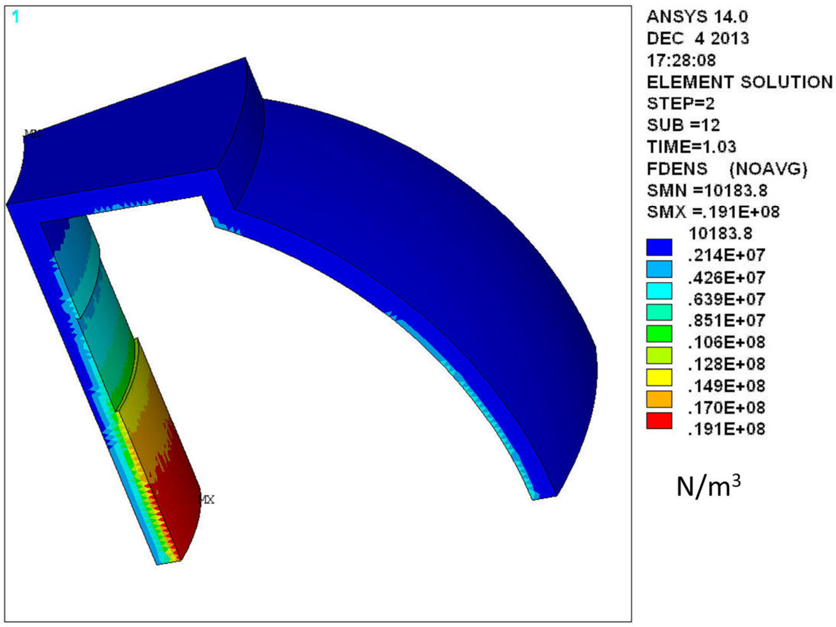

Fig. A6. Radial magnetic body force on Structural Ring at t=1.03 s.

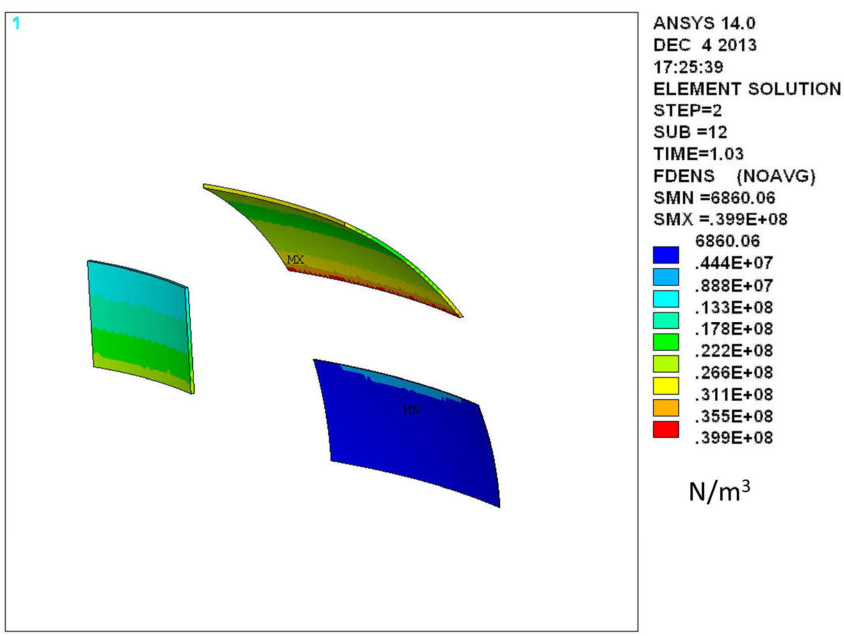

Fig. A7. Radial magnetic body force on Stabilizing Ring at t=1.03 s.

References

1. The ARIES Project: http://aries.ucsd.edu/ARIES/.
2. M.S. Tillack, S. Malang, L. Wagner, X.R. Wang, D.K. Sze, L. El-Guebaly, C.P.C Wong, J.A. Crowell, T.K. Mau, L. Bromberg, and the ARIES Team: "Configuration and Engineering Design of the ARIES-RS Tokamak Power Plant," *Fusion Engineering and Design*, **38**(1997) 87-113.
3. H.H. Toudeshki, F. Najmabadi, X.R. Wang and the ARIES Team, "Vacuum Vessel Analysis and Design for the ARIES-ACT1 Fusion Power Plant," *Fusion Science and Technology*, **64**(3), 675-679, 2013.
4. Pathak, H.A.; Raval, J.R.; Phull, G.S.; Laad, R.; Wang, X.; Ioki, K.; Suresh, P.V.S., "Manufacturing of ITER vacuum vessel In-Wall Shielding," *2013 IEEE 25th Symposium on Fusion Engineering (SOFE)*, (2013), 1-6.